Experimental Mechanics (2010) 50:1335–1348
DOI 10.1007/s11340-010-9351-5

Effects of Body Cross-sectional Shape on Flying Snake Aerodynamics

K. Miklasz · M. LaBarbera · X. Chen · J.J. Socha

Received: 24 July 2009 / Accepted: 24 March 2010 / Published online: 14 April 2010

Abstract Despite their lack of appendages, flying snakes (genus *Chrysopelea*) exhibit aerodynamic performance that compares favorably to other animal gliders. We wished to determine which aspects of *Chrysopelea*'s unique shape contributed to its aerodynamic performance by testing physical models of *Chrysopelea* in a wind tunnel. We varied the relative body volume, edge sharpness, and backbone protrusion of the models. *Chrysopelea*'s gliding performance was surprisingly robust to most shape changes; the presence of a trailing-edge lip was the most significant factor in producing high lift forces. Lift to drag ratios of 2.7–2.9 were seen at angles of attack (α) from 10–30°. Stall did not occur until $\alpha > 30°$ and was gradual, with lift falling off slowly as drag increased. *Chrysopelea* actively undulates in an S-shape when gliding, such that posterior portions of the snake's body lie in the wake of the more anterior portions. When two *Chrysopelea* body segment models were tested in tandem to produce a two dimensional approximation to this situation, the downstream model exhibited an increased lift-to-drag ratio (as much as 50% increase over a solitary model) at all horizontal gaps tested (3–7 chords) when located slightly below the upstream model and at all vertical staggers tested (±2 chords) at a gap of 7 chords.

Keywords Gliding · Flight · Animal locomotion · Snake · Aerodynamics

Introduction

'Flying' snakes (genus *Chrysopelea*) glide like no other animal. With no appendages or membranes to use as lift-generating surfaces, *Chrysopelea* instead flattens its body and glides using their body as a single 'wing'. In flight, these snakes simultaneously send traveling waves from head to tail and oscillate the posterior body and tail in the vertical plane; the body's three-dimensional posture constantly changes during the glide. Despite their highly unconventional and dynamic mode of gliding, aerial performance of gliding snakes is on a par with or surpasses that of many other gliding vertebrates. For example, the paradise tree snake (*Chrysopelea paradisi*) can glide at 13° below horizontal, comparable to some gliding lizard species (genus *Draco*, [1]) and shallower than reported in some gliding squirrels [2–7] and gliding ants [8]. Although the kinematics of snake gliding has been previously characterized [9–11], nothing is known about how these snakes produce aerodynamic forces using a combination of morphology and behavior that is so dramatically different from other gliders.

Along with its continuously changing body posture, the cross-sectional shape of a flying snake's body is likely to have a major influence on its aerodynamic performance.

Michael LaBarbera and John J. Socha contributed equally to this work.

K. Miklasz · M. LaBarbera
Department of Organismal Biology and Anatomy,
University of Chicago,
Chicago, IL 60637, USA

X. Chen · J.J. Socha (✉)
Department of Engineering Science and Mechanics,
Virginia Tech,
Blacksburg, VA 24061, USA
e-mail: jjsocha@vt.edu

Present Address:
K. Miklasz
Hopkins Marine Station, Stanford University,
Pacific Grove, CA 93950, USA

Upon launching itself from the substrate, *C. paradisi* alters its cross-section to a shape that is markedly flatter and wider than a typical snake's rounded cylindrical body (Socha in prep). In this 'flattened' configuration [Fig. 1(h)], the width of the body is doubled; the increase in the snake's planform area presumably increases lift. As the body widens, it flattens dorsoventrally (i.e., along the back-belly axis, analogous to a cobra flattening), reducing the projected profile perpendicular to the direction of airflow and thus presumably decreasing drag [12]. This body shape change results in an 'airfoil' with the following characteristics: 1) a recessed, flattened ventral (bottom) surface; 2) a roughly triangular dorsal (top) surface with a protruding, rounded apex, produced by the slightly projecting backbone; and 3) ventrally-projecting 'lips' on each lateral edge formed from marginal scales [Fig. 1(g, h)]. Because the snake glides with the body extended in cross-wind loops, the body 'airfoil' also exhibits fore-aft symmetry (Socha in prep). If and how each of these features affect the snake's gliding performance is unknown. Further complicating the analysis, the traveling waves that move posteriorly down the body ensure that some portion of the snake's posterior body always lies downstream of a more anterior portion. This configuration is likely to produce aerodynamic interactions between the upstream and downstream body segments, but whether those effects are beneficial or detrimental is also unknown.

In this study, we used physical and computational modeling to address two questions about the effects of gliding snakes' morphology and behavior on their aerodynamics—(1) the effects of cross sectional shape, and (2) the interaction of the downstream body segment with the wake of the upstream segment.

Which major aspects of *Chrysopelea*'s cross-sectional shape are functionally important, and how do they contribute to lift and drag production? We hypothesized that the shape of the snake's ventral surface, in particular the symmetric ventrally projecting lips, increases lift by producing a sharp trailing edge regardless of which side of the body is the leading edge. In contrast, we hypothesized that the protrusion of the backbone on the dorsal surface has a detrimental effect on flight performance—at low and moderate angles of attack, the backbone protrusion increases the projected area of the body segment and may also fix the location of flow separation (increasing the depth of the wake); both effects will increase drag.

Aerial undulation places large sections of the body perpendicular to the oncoming air flow, but positions more posterior regions of the body in or near the wake of upstream regions. What is the effect of the interaction between an upstream body segment's wake and the downstream body segment? We hypothesized that the lift-to-drag ratio of the downstream body segment will be reduced when it is located in the wake

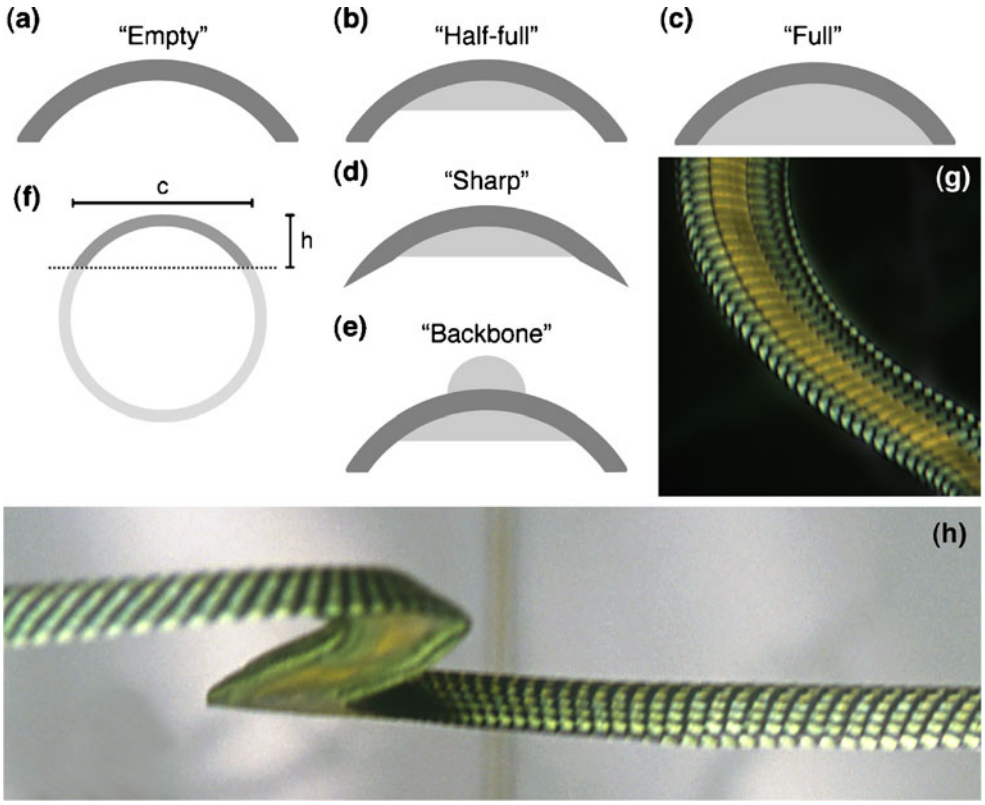

Fig. 1 (**a**–**e**) Cross-sectional shapes tested in this study, depicted at scale. The 'half-full' model most closely resembles the mid-body cross-sectional shape of the flying snake *Chrysopelea paradisi* while gliding, seen in photos in (**g**) and (**h**) (from Socha, in prep). Panel (**f**) depicts the horizontal cut used to create the base cylindrical section of each physical model, and defines the model dimensions chord, c, and height, h

of the upstream segment. Because this study represents the first attempt to quantify any aspect of gliding snake aerodynamics, we conducted simple static modeling and treated the body segments as infinite straight sections, ignoring potential complicating factors such as body movement, curved portions of the body, and surface texture due to scales.

Methods

The primary data in this study were obtained from physical models. We tested model flying snake body segments in a wind tunnel located in the Department of Geophysical Sciences at the University of Chicago. In a first set of experiments, we tested the effects of various aspects of cross-sectional shape on a single model, measuring lift and drag forces at multiple angles of attack. Specifically, we varied the relative body volume, the sharpness of the lateral edges, and the presence of a protrusion on the dorsal surface. In a second set of experiments, we determined the effects of positioning a snake body segment model in or near the wake of another, upwind body segment by positioning two models in the wind tunnel in tandem. We varied the relative position—both horizontal separation ('gap') and vertical displacement ('stagger')—of the two models while measuring the forces on the downstream model. Additionally, we visualized the flow at points of interest in both sets of manipulations.

Physical Models

Physical models representing a body segment of *Chrysopelea* were custom-made from lengths of aluminum tubing (tubing diameter, 5.08 cm; length, 33 cm; wall thickness, 3.2 mm); schematics of the model cross-sections are shown in Fig. 1(a-e). The approximate curvature and depth of the snake's cross-sectional shape were emulated by cutting the tubing lengthwise along a chord [Fig. 1(f)]. The resulting shape had a cross-section with a height of 1.27 cm and width (= chord) of 4.39 cm (aspect ratio = 7.5); the chord was about twice that of a typical *Chrysopelea paradisi* adult. The cut edges were rounded by light sanding with sandpaper. The ends of the models were capped with aluminum discs [diameter, 5.08 cm; thickness, 6 mm; Fig. 2(d)] to permit convenient rotation of the model and to inhibit air flow around the ends of the model from the under to the upper side. Filler pieces were cut from an acrylic cylinder (cylinder diameter, 4.4 cm) to produce the 'half-full' [0.42 cm deep filler; Fig. 1(b)] and 'full' [0.95 cm deep filler; Fig. 1(c)] models.

The model that most closely resembled a real flying snake's cross-sectional shape at mid-body during a glide [Fig. 1(h)], the half-full version [Fig. 1(b)], was considered the base model. Relative body volume was varied by taking out the acrylic filler to produce the 'empty' model [Fig. 1(a)], or by inserting the larger acrylic segment for the 'full' model [Fig. 1(c)].

For one model, we modified the edges of the aluminum tubing segments to change lip sharpness [Fig. 1(d)]. The edges of this 'sharp' model were produced by grinding a diagonal flat 0.6 cm long along both inner surfaces of the segment at an angle that terminated the flat at the level of the ventral surface of the filler piece for the half full model.

As an additional variant, the effect of backbone protrusion was simulated by adding brass half-tubing to the center of the top surface of the base model [Fig. 1(e)]. Brass tubing (tubing diameter, 1.2 cm; wall thickness, 0.4 mm) was cut in half lengthwise and used to model the dorsal protrusion of the backbone. To magnify this effect, we deliberately chose tubing that was proportionately larger than the equivalent morphology in the real snake.

Wind Tunnel

The wind tunnel was a suction-type, open-circuit tunnel with the impeller located at the downstream end; a 150 cm long bell on the upstream end (contraction ratio, 18.5:1) led into a 34 cm tall × 36 cm wide cross section tunnel, 7.6 m long [Fig. 2(a)]. A hexagonal close-packed array of soda straws downstream of the bell served as a flow straightener (collimator) to damp ambient turbulence; models were tested 2.1 m downstream from the collimator. The mean freestream turbulence intensity was no more than 2% of the freestream velocity. The models spanned virtually the entire width of the wind tunnel (99.4%) to minimize edge effects [Fig. 2(c, d)].

We maintained dynamic similarity by choosing a model Reynolds number within the range experienced by gliding snakes [11]. Reynolds number (Re), a quantity proportional to the ratio of inertial to viscous forces, is defined as:

$$\mathrm{Re} = \frac{\rho D U}{\mu} \tag{1}$$

where ρ is air density, μ is the dynamic viscosity of air, D is a characteristic length, and U is air speed. Following Socha et al. [11], we chose the chord of the model, representing the width of an airborne snake, as the characteristic length. The chord of our models was about twice the width of a real adult *Chrysopelea*'s body. With reported Reynolds numbers of 5,000–15,000 [11], to maintain dynamic similarity we chose a wind tunnel speed (6.1 ms^{-1}) roughly half of the reported glide speed of *Chrysopelea paradisi* (range, 10–12 ms^{-1}), yielding a Re of 15,000 for the models.

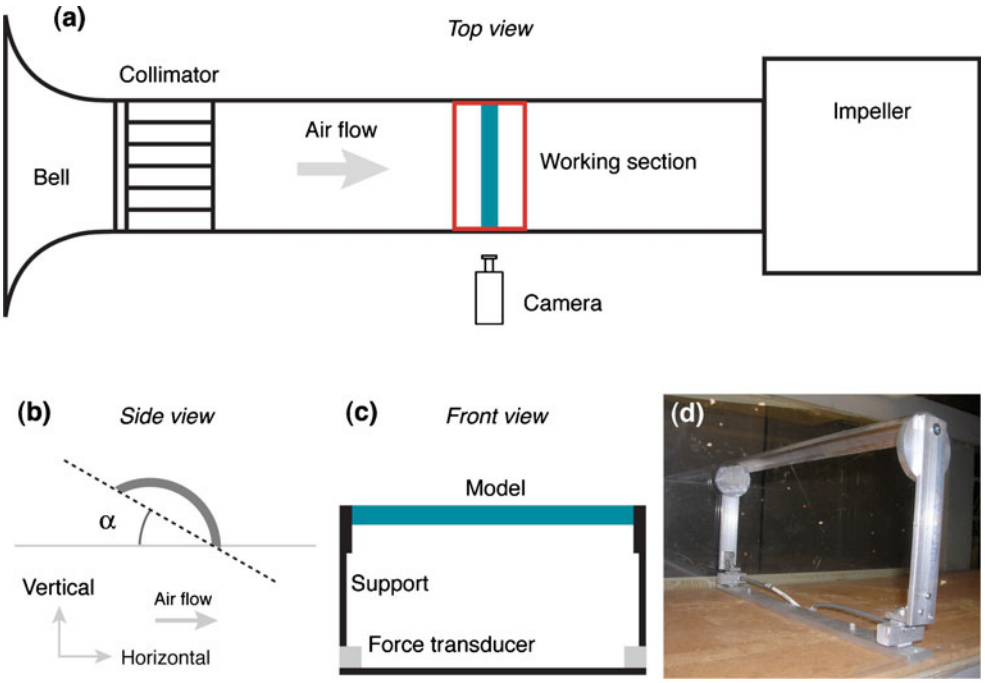

Fig. 2 Experimental setup for wind tunnel testing. (**a**) Schematic of the wind tunnel in top view. The arrow depicts the direction of air flow. (**b**) Definition of angle of attack, α, relative to the freestream air flow. (**c**) Schematic of the working section in front view. Note that (**a**–**c**) are not to scale. (**d**) Photo of a model mounted in the working section, showing the end caps, vertical stings, and force transducers in place (In the setup figured, the force transducers would measure lift forces)

Force Measurement

We measured lift and drag forces in separate trials. Two full bridge strain gauge force transducers (OmegaDyne Model LC703–10, Sunbury, Ohio, USA) were used to measure forces. The force transducers were located at the bases of the vertical stings that secured the model to the wind tunnel floor, and were re-oriented depending on whether lift or drag forces were being measured. The output from the force transducers was amplified using a Vishay Micro-Measurements Strain Gage Conditioner, Model 2120B (Malvern, Pennsylvania, USA) and digitized using a GW Instruments InstruNet Model 100 analog-to-digital converter (Somerville, Massachusetts, USA). The data were recorded on an Apple Powerbook G3 laptop computer. Because we were solely interested in time-averaged measurements, data were sampled at 5 Hz and recorded for 10–20 s. The system was calibrated by placing known masses (2–100 g) on the force transducers. The standard error of the mean for both the lift and drag force measurements was 1.7 mN, representing 0.34% and 0.40% relative to full scale (500 mN for lift, 425 mN for drag), respectively.

We accounted for forces on the stings by measuring drag and lift forces in the absence of a model. Lift was negligible; drag was 29±3.4 mN (mean±standard deviation of eight measurements) and was subtracted from all raw drag measurement values. Average drag on the stings represented roughly 20% of the measured drag force of the half-full model at α=0°, and 5% at α=50°.

For each model, we measured lift and drag forces at angles of attack between −10° and +50°, at 5° intervals. Angle of attack (α), defined as the angle between the chord and the freestream airflow [Fig. 2(b)], was determined manually using a protractor glued to the end of the model; the model was rotated to the desired angle (relative to the floor of the wind tunnel) and locked in place with set screws in the vertical stings. A laser was later used to determine the accuracy of this method. The largest source of error resulted from misalignment when gluing the protractor to the model; this error was up to 1°. Because this error was systematic for any given model, the shape of individual polar plots of lift and drag were not affected. Manual adjustment of angle of attack from trial to trial within a model produced a smaller random error of ±0.1°.

From the force measurements, we calculated time-averaged lift and drag coefficients as follows:

$$C_L = \frac{2F_L}{\rho A U^2} \tag{2}$$

$$C_D = \frac{2F_D}{\rho A U^2} \tag{3}$$

where C_L and C_D are lift and drag coefficients, F_L and F_D are lift and drag forces, ρ is air density, A is planform area, and U is air speed. Using propagation of errors, the relative error of lift and drag coefficients was determined to be 6.5% at full scale, resulting largely from the uncertainty in the wind tunnel speed (0.2 m/s).

Tandem Models

In a second set of experiments, we used a pair of models in tandem to simulate statically the upstream and downstream body segments of an undulating, airborne snake. The upstream model was used to create a wake, and forces were measured on the downstream model (only) as before. The relative position of the models was varied by repositioning the upstream model vertically (stagger) in 1 cm increments (±8 cm) or horizontally at spacings (gap) of three, five, and seven chord lengths (13.5, 22.5, and 31.5 cm) between trials. All combinations of gap and stagger were tested. Both upstream and downstream models were the 'empty' versions, and both were oriented at an angle of attack of 25°. This angle was chosen arbitrarily from the range of body orientation angles reported by Socha et al. [11]. Angle of attack of real gliding snakes varies continuously with time and position along the body, an effect not considered here.

Flow Visualization

To visualize general flow patterns around the models, we seeded the airflow with lycopodium spores and used a laser line generator to illuminate the particles in a plane perpendicular to the axis of the model (parallel to the airflow). The laser line generator (Lasiris Inc. Magnum 750 mW, wavelength = 670 nm) was mounted 10 cm above the wind tunnel and projected a sheet of light downward through the acrylic upper wall. Movies of flow patterns were recorded with a high definition video camera (HDR-HC1, Sony, Tokyo, Japan) [Fig. 2(a)]. The shutter speed was set to a relatively long duration (0.1 s) so that particle paths were recorded as streaks (pathlines) across the image.

Computational Modeling

Our initial analyses of the physical model data motivated us to conduct further testing using computational methods. We tested the empty, half-full, and full cross-sectional shapes using two-dimensional modeling. The purpose of these trials was twofold. The primary motivation was to validate the force coefficients attained from the physical models. Although we aimed to isolate 2D effects of cross-sectional shape, the physical models may have exhibited 3D effects given the models' relatively low aspect ratio (7.5) and lack of true end plates. Computational modeling thus served to evaluate if these issues were a problem. Our secondary motivation was to extend the range of angle of attack beyond 50° to explore the full range of force coefficients experienced by the snake.

Simulations were performed with the commercial computational fluid dynamics (CFD) software Fluent (Ver. 6.3) using a pressure-based model with coupled calculations of pressure and velocity. Models were meshed with Gambit software (Ver. 2.4.6). The computational domain was defined to be 30× in length and 15× in height relative to the chord width of the snake model (4.4 cm). Due to strong interactions between the mean flow and turbulence, the numerical results for turbulent flows tend to be more susceptible to grid dependence than those for laminar flows. Therefore, regions where the mean flow gradients were high were resolved with correspondingly finer meshes. Boundary layer meshes were constructed along the perimeter of the airfoil to capture these steeper flow gradients; quadrilateral meshes were used throughout the domain. Specifically, there were 100 nodes on the top and bottom of the airfoil, with the height of the first layer of grid lines at 0.025 cm (about half the width of the cell). To maintain Reynolds number similarity with the wind tunnel experiments (Re=15,000), we used the same model width (4.4 cm) and air velocity at far field (6.1 m/s), and we used 1.225 kg/m^3 and 1.7894e–05 kg/ms for the density and dynamic viscosity of air, respectively. Because the snake's Mach number was very low (<0.02), we assumed the air to be incompressible with constant viscosity; heat transfer was ignored.

The Fluent simulations employed the two-dimensional Reynolds-averaged Navier-Stokes (RANS) equations. The Spalart-Allmaras (SA) model [13] was chosen to model viscous effects. SA is a relatively simple one-equation model for the turbulent viscosity, but it has been shown to yield reasonable results for boundary layers subject to adverse pressure gradients. The transported variable in the SA model is the modified turbulent kinematic viscosity, which was set to zero at the walls. To ensure accuracy, we chose second-order upwind schemes for both momentum equations and modified turbulent viscosity. We note that at the Reynolds number studied here (Re=15,000), the flow may not be fully turbulent. However, the laminar solver that we used initially proved insufficient, because trials with angles of attack beyond 25° failed to converge. In contrast, the SA model produced convergent results for all cases. This is one advantage of the SA model, which was initially proposed to resolve low Reynolds number flow—this model integrates down to the boundary wall and is designed for adverse-pressure gradients during separation, and separation always occurred for each of our tested cross-sectional shapes. Lastly, we note that at angles of attack below 25°, the force coefficients yielded by the laminar and turbulent solvers were quite similar, differing by less than 10%.

We initially used a steady-state model for each simulation from $\alpha=-10°$ to 75° in 5° increments. Simulations from $\alpha=80°$ to 90° did not converge and therefore are not reported. Motivated by the sharp transition in the lift and drag coefficients at $\alpha=30°$ in the experimental data [e.g., Fig. 3(a)], we conducted additional simulations using an

unsteady model. To ensure fast and convergent solutions, we used the steady-state velocity and pressure fields as initial conditions. A first-order implicit scheme was employed for time stepping, with initial steps as small as 2.5e–5 s. This small time step ensured that the air traveled less than one grid dimension, so that the highest frequencies of the (developing) turbulence were captured. For angles of attack between 0° and 30°, the unsteady simulations converged to the steady-state solution for all three modeled cross-sectional shapes. For all other angles of attack, we report results from the unsteady simulations.

Results

Lift and Drag Forces

For all physical models tested, at negative angles of attack (−10° to 0°) the lift and drag coefficients were relatively small and changed little with angle of attack [Fig. 3(a, b)]. Above 0°, lift and drag both increased with increasing angle of attack. This trend continued until the stall angle (defined as the angle of attack at which maximum lift is achieved) was reached at α=30°. With further increases in angle of attack, lift decreased slightly while drag increased rapidly. Between 25° and 30°, lift increased while drag remained the same [Fig. 3(a, b)], resulting in an apparent spike in the polar plots [Fig. 4(a, b)]. This feature was not seen in the computational results [Figs. 3(c, f) and 4(c)]; the numerical simulations produced much smoother transitions for lift and drag around α=30°. The maximum lift occurred at 30° in the numerical simulations, in agreement with the physical modeling. The maximal lift to drag ratio (L/D) ranged between 2.7 and 2.9 for all models. Near-maximal L/D ratio occurred over a wide range of angles of attack, from 10° to 30° in the physical models [Fig. 3(d, e)] and from 10° to 25° in the computational models [Fig. 3(f)].

Flow Visualizations for Solitary Model

From the polar plots of the physical models (Fig. 4), we distinguish three broad regions of characteristic aerodynamic performance: near-constant force coefficients (α=−10° to 0°), pre-stall, where C_L increases rapidly and C_D increases slowly (α=0° to 30°), and post-stall, where C_L decreases slowly but C_D increases rapidly (α=30° to 50°). Observations of the flow patterns that characterize these three regions (Fig. 5) help explain the observed trends in the force coefficients.

The near-constant region (α=−10° to 0°) was characterized by small drag coefficients and relatively constant, negative lift coefficients. At these low angles of attack, the flow separated from the upper surface of the model near the highest point of the profile (the midpoint of the chord), and separated from the bottom of the model at the leading edge [Fig. 5(b)]. A wake only slightly wider than the streamwise projection of the model corresponded to the relatively small measured drag forces, and the wake's vertical symmetry corresponded to the small measured lift forces.

The pre-stall region (α=0° to 30°) was characterized by an increase in both lift and (to a much smaller degree) drag with increasing angles of attack. The flow pattern over the top of the model was qualitatively similar to that seen at non-positive angles of attack, with separation occurring at approximately the highest point of the profile [here approximately a quarter of the chord from the leading edge; Fig. 5(c)]. The flow on the underside of the model again separated from the leading edge, but in this case the air flow was additionally deflected downwards by the trailing edge of the airfoil, a major modification of the pattern seen at non-positive angles of attack [Fig. 5(c)]. The downward deflection of the pathlines likely caused the large increase in measured lift force, and produced a deeper wake which likely increased measured drag forces. The downward deflection of the airflow qualitatively increased with angle of attack.

The post-stall region (α=30° to 50°) was characterized by a small decrease in measured lift and a large increase in measured drag with increasing angles of attack. Flow separated from the leading edge of the model's upper surface and was deflected strongly upward [Fig. 5(d)], creating a deep wake correlated with the large calculated drag coefficients. Further increasing the angle of attack increased the depth of the wake without noticeably increasing the downward deflection of the air, which corresponds to the observed increase in drag and little change in lift with increasing angle of attack.

Effects of Ventral (Bottom Surface) Profile

The effect of relative body volume was tested using empty, half-full, and full models. The empty and half-full models showed nearly identical lift and drag characteristics at all angles of attack [Figs. 3(a, d) and 4(a)]. In contrast, the full model differed drastically from the other two models. At all angles of attack greater than 0°, lift and drag coefficients were lower in the full model than in the half-full or empty models [Fig. 3(a, c)]. L/D ratio was also lower in the full model than in the other two models for α=0° to 25°, although the maximum L/D ratio and the stall angle are similar in the two models [Fig. 3(d)].

Relative edge ("lip") sharpness had little effect on the aerodynamic characteristics. The aerodynamic performance

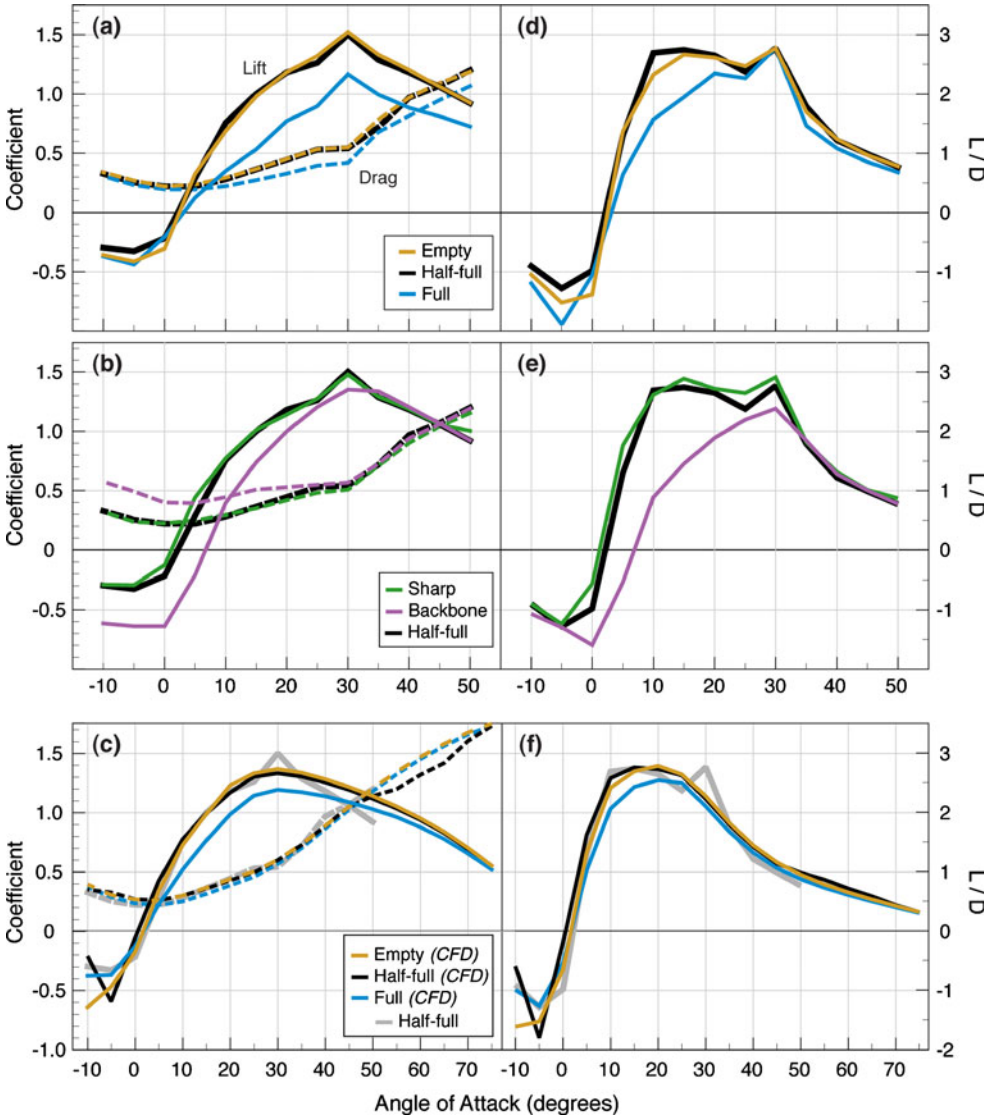

Fig. 3 Lift and drag characteristics vs. angle of attack for all models. Lift and drag coefficients are plotted in (**a**–**c**), with lift represented by solid lines and drag represented by dashed lines; corresponding lift-to-drag (L/D) ratios are plotted in (**d**–**f**). (**a**, **d**) Comparisons of the empty and full models to the half-full model. (**b**, **e**) Comparisons of the sharp edge and backbone models to the half-full (= rounded edge) model. (**c**, **f**) Computational modeling results. For reference, the results for the half-full physical model are also shown (in gray)

of the sharp model was similar to the half-full model with rounded edges [Figs. 3(b, e) and 4(b)] and polar plots for these models were nearly identical [Fig. 4(b)].

Effects of a Dorsal (Top Surface) Protuberance

The 'backbone' model displayed much greater (and near-constant) drag and slightly lower lift [Fig. 3(b) and 4(b)] than the half-full model at each angle of attack between 0° and 30°. Both the backbone and the half-full model had the same stall angle, 30°, and performed similarly at post-stall angles of attack. The maximum lift coefficient and maximal L/D ratio were smaller for the backbone model [Fig. 3(e)]; L/D ratio peaked sharply over a very narrow range of angles of attack (25° to 30°), unlike the 20° range (α=10° to 30°) of near-maximal L/D ratio in the base (half-full) model [Fig. 3(e)].

Tandem Models

We positioned models in tandem—upstream and downstream—and measured aerodynamic forces on the downstream model. When the downstream model was positioned directly behind the upstream model (stagger = 0; 'drafting'), the drag coefficient of the downstream model (based on free-stream airspeed) markedly decreased [Fig. 6(a)] relative to a solitary model at the same angle of attack (25°). The effect of drafting decreased as the gap increased. As the stagger increased (either in the positive or negative direction), the drag coefficients of the downstream model approached those of a solitary model.

The lift coefficient of the downstream model exhibited a more complicated relationship with relative position [Fig. 6(b)]. When the downstream model was directly behind the upstream model (stagger = 0), the calculated

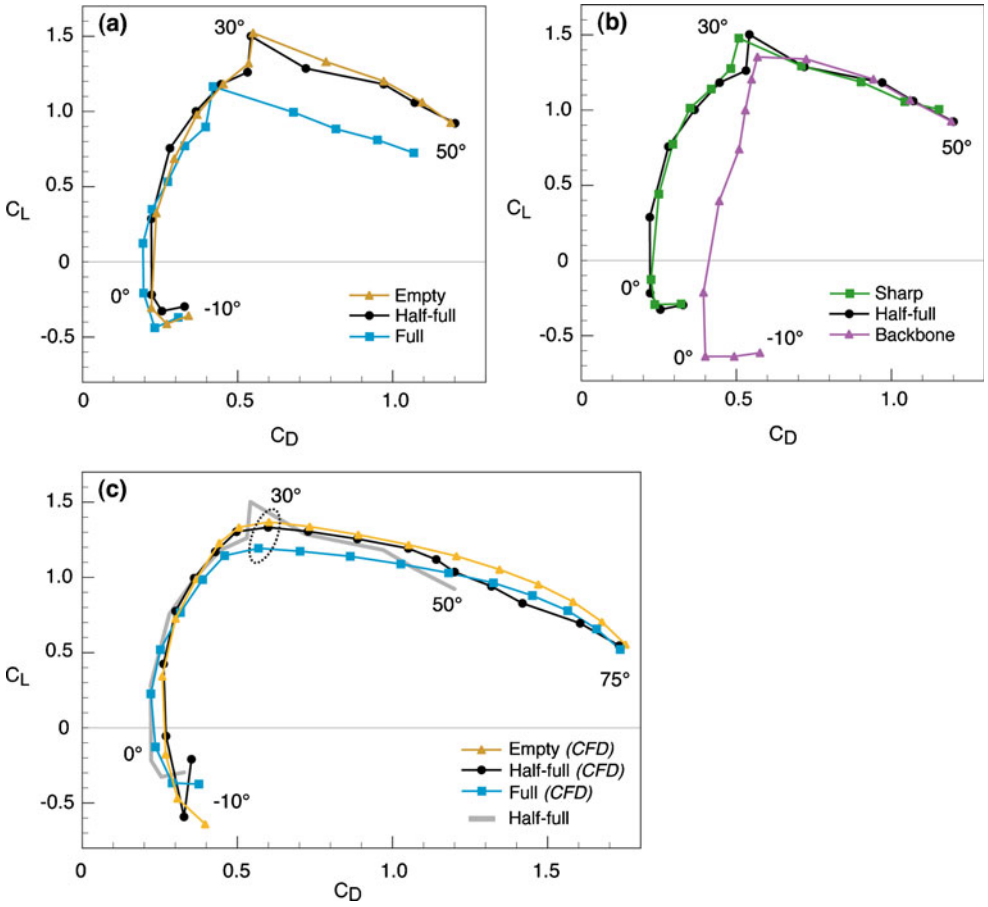

Fig. 4 Polar plots of lift and drag coefficients for all models. Data are plotted in 5° increments of angle of attack. (**a**) Comparison of the empty and full models to the half-full model. (**b**) Comparison of the sharp and backbone models to the half-full model. (**c**) Computational modeling results. For reference, the results for the half-full physical model are also shown (in gray)

lift coefficient (based on free-stream airspeed) decreased markedly. The reduction in lift coefficients (up to 50% relative to a solitary model) associated with drafting was rapidly attenuated with increasing separation between the models, although lift coefficients remained about 20% lower than was seen in comparable solitary models. When the downstream model was positioned higher than the upstream model (above its wake), lift coefficients asymptotically approached a solitary model's lift coefficient. When the downstream model was positioned lower than the upstream model (below its wake), lift coefficient reached values 26% *larger* than those of a solitary model [Fig. 6(b)]. This apparent lift augmentation was present at horizontal separations of three and five chord widths, but not at seven chord widths.

The lift-to-drag ratio for the downstream model in a tandem model system is plotted in Fig. 6(c). For all horizontal separations tested, L/D ratio was highest when the downstream model was slightly (0.5–1.5 chord widths) below the upstream model. L/D ratio ranged from lower to higher than a solitary model when the downstream model was positioned above the upstream model. The L/D ratio was lowest when the downstream model was slightly (0.5 chord widths) higher than the upstream model and the models were separated by three chord widths. Interestingly, when separated horizontally by seven chord widths, the downstream model experienced increased L/D ratios at all vertical displacements [Fig. 6(c), light gray].

Discussion

General Aerodynamic Characteristics

Chrysopelea models perform well as an airfoil, and their performance at realistic orientations is impressively robust; i.e., insensitive to small perturbations in angle of attack. The polar plots imply a high stall angle, a gentle drop in lift after stall, and a broad range of angles of attack with near maximal L/D ratio. The range of angles of attack with high values of L/D ratio is particularly impressive; a flying snake can glide at any angle of attack between 10° and 30° and still achieve a high L/D ratio. Conversely, there is a steep gradient of L/D ratio at lower angles of attack; a body segment that rotated from α=10° to 0° would experience a range of L/D ratios that spans best to worst values. Although ostensibly detrimental, the snake may take advantage of this sensitive angle of attack range for control

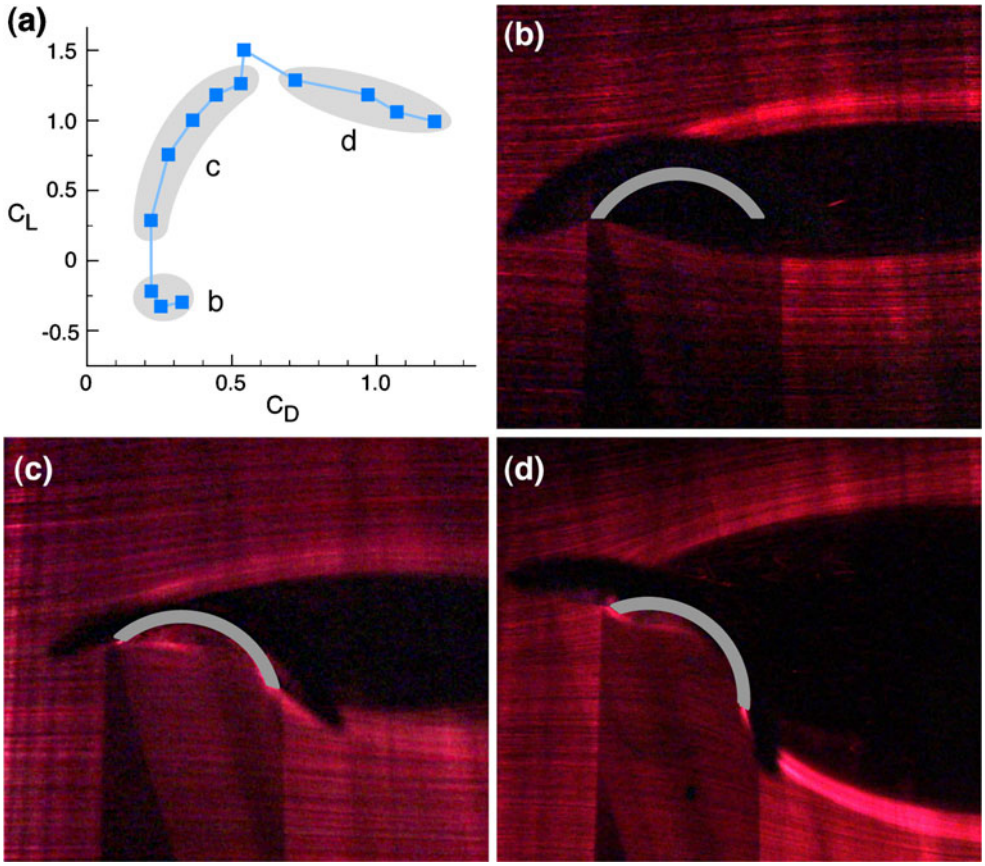

Fig. 5 Flow visualizations from a solitary model. Images in (**b**–**d**) are representative video stills chosen from the three characteristic regions indicated in grey in the polar plot (**a**). Angle of attack: (**b**) $\alpha=0°$; (**c**) $\alpha=15°$; (**d**) $\alpha\cong35°$. Note: the laser sheet used to illuminate the particles was located midway along the length of the model. The large curved dark shadow is the model edge at the near-wall of the flow tank, closest to the videocamera, and therefore appears larger than the actual cross-section at the laser (*shown in gray*)

purposes. We were particularly surprised to see that these polar plot features were robust with respect to many aspects of cross-sectional shape.

Effects of Ventral Wing Profile

Most variations tested with respect to body volume and edge sharpness were similar in aerodynamic performance (Figs. 3 and 4). The half-full model is most similar to a flying snake's actual cross section; the polar plots of most shape variants tested were generally similar to this 'base' model.

The model without lateral lips (the full model) produced lift and drag forces at all angles of attack that were smaller than any of the models with a lip [the half-full and empty models, Fig. 3(a)], regardless of lip shape [the sharp or rounded models, Fig. 3(b)]. The shift from a full (and cylindrical) to half-full shape is one consequence of the snake expanding its ribcage; in addition to increasing the planform area of the body, ribcage expansion indirectly generates the lateral lips by its interaction with the lateral scales. The nearly identical polar plots of the half-full and empty models (and of both lip-shape variants) suggest that one of the critical factors determining aerodynamic performance in flying snakes are the lips themselves. At angles of attack equal to or less than zero, all models (except the 'backbone' model) performed identically in terms of lift and drag coefficients; it is only at positive angles of attack that the full model began to exhibit differences from the other models. At positive angles of attack below stall in models with lips, the flow separated from the ventral surface at the leading-edge lip, reattached to the ventral surface at some point downstream, and then was strongly deflected downward by the trailing-edge lip [Fig. 5(c)]. Note that the angle that the trailing-edge lip makes to the oncoming flow will always be greater than the angle between a flat ventral surface and the flow; a model with lips will always deflect the airstream downward more strongly than a model without lips at positive angles of attack. The downward-directed momentum transfer to the air implies higher lift coefficients in lipped models, with the discrepancy between lipped and lipless models increasing with increasing angle of attack [Fig. 3(a)]. Consistent with this interpretation, note that the full (i.e., lipless) model exhibits slightly *smaller* drag coefficients than lipped models, with the discrepancy between lipped and lipless models increasing with increasing angle of attack. This interpretation suggests that the trailing edge lip is critical but that the leading edge lip is not. Consistent with this interpretation, previous work has found that both lift and drag coefficients increase with the addition of leading and trailing edge flaps, and that the effect of the trailing edge is

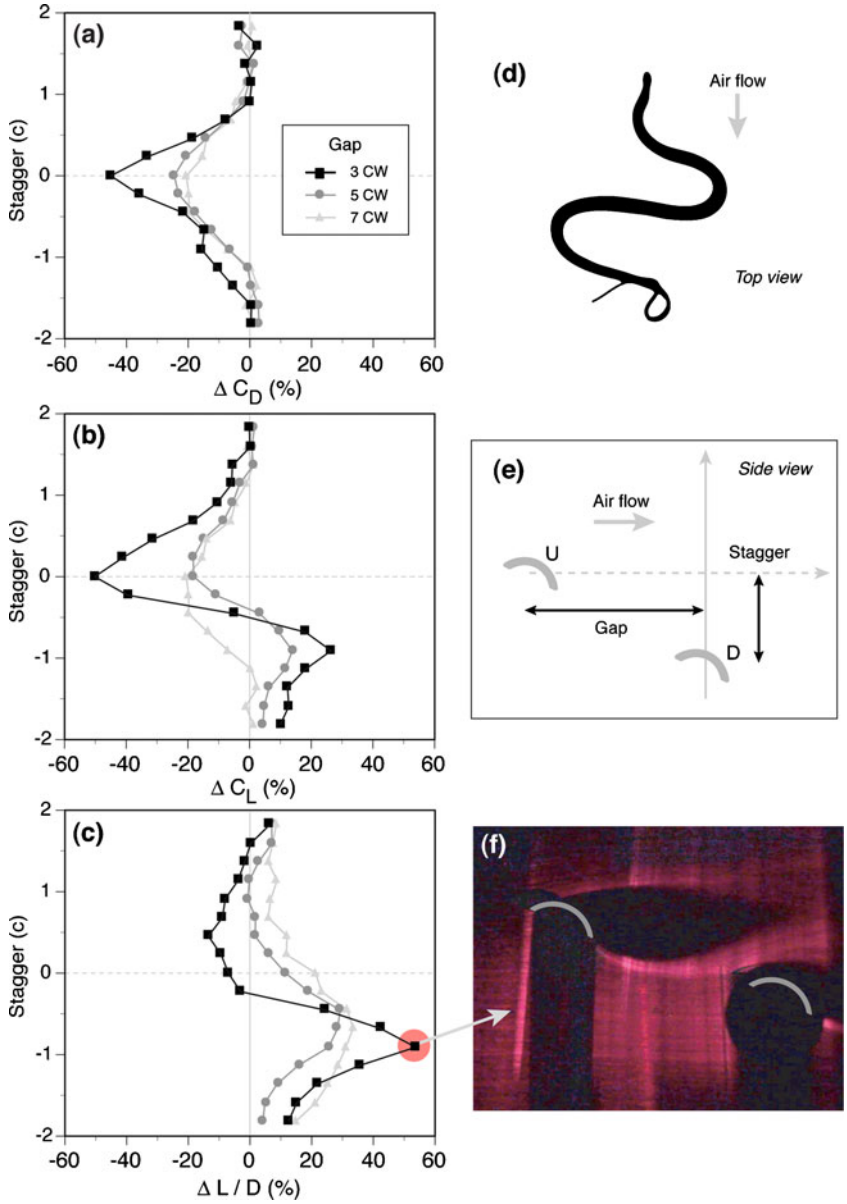

Fig. 6 Relative lift and drag coefficients and L/D ratios for the downstream model from the tandem model trials. Graphs (**a**–**c**) show the relative change in drag coefficient (**a**), lift coefficient (**b**), and lift-to-drag (L/D) ratio (**c**) of the downstream model compared to a single model at the same angle of attack (α=25°) as a function of the position of the downstream model. For each graph, the percent change relative to a solitary model is plotted against vertical displacement (stagger) from the level of the upstream model, measured in chords (1 c=4.4 cm). These tandem manipulations modeled two flying snake segments oriented orthogonally to the oncoming air flow, as exemplified in the top-view silhouette of a snake in mid-glide (**d**). In this posture, the tandem models represent the first two orthogonal body segments. For reference, the snake's head is at the top and its tail is at the bottom; the tail is curling over the rear body segment. (**e**) Definitions of stagger and gap. 'U' and 'D' indicate the upstream and downstream segments, respectively. (**f**) Flow visualization from the model configuration that yielded the maximum increase in both lift coefficient and L/D ratio, as indicated in (**c**)

much stronger (e.g., [14], Fig. 6–23). The effect of flaps is typically tested at Reynolds numbers of at least 10^6; further work is needed to characterize the apparently similar effect in the Reynolds number range of flying snakes.

Lastly, we note that in addition to differences in aerodynamic characteristics, the differences in shape between full and lipped configurations may have implications for the snake's structural characteristics (such as strength and stiffness). Such issues of aeroelasticity will be addressed in future studies.

Effects of Dorsal Wing Profile

The model bearing a dorsal protuberance ('backbone') is an obvious outlier from the other models in the shape of the polar plot, with the 'backbone' model producing lower lift forces and higher drag forces at all angles of attack lower than the stall angle [Figs. 3(b, e) and 4(b)].

The higher measured drag in the backbone model is consistent with the flow patterns we observed in other models. In the pre-stall region (α=0° to 30°), flow presumably separates from the model at the highest point in the profile, the dorsal protrusion, producing a wider wake in the backbone model, which in turn would cause the model to experience greater drag. In the post-stall region (α=30° to 50°), the angle of attack is sufficiently large that the backbone would lie in the wake where its presence could have no effect on the point of separation. As expected under this interpretation, once the dorsal protuberance is buried in the wake (post-stall), the drag coefficient of the

backbone model is identical to those of the other models [Figs. 3(b) and 4(b)]. The "backbone" protuberance was deliberately exaggerated in our model since we were interested in exploring the extremes of morphological variation. In reality, *Chrysopelea* likely experiences drag coefficients intermediate between those of the base model and the backbone model at moderate angles of attack.

One curious feature of the physical model data is the jump in lift coefficient from $\alpha=25°$ to $\alpha=30°$, an effect not seen in the computational models. Spedding et al. [15] found a similar discontinuity in their study of the Eppler 387 airfoil at Reynolds numbers from 10,000 to 60,000. They report a dramatic increase in lift coefficient and decrease in drag coefficient at one angle of attack (from roughly $\alpha=5°$ to 10°) when Re>30,000. They attribute this feature to a (dorsal) laminar separation bubble, a characteristic of moderate Reynolds number flows [16]. A separation bubble occurs when the laminar flow over the leading edge separates from the upper surface and creates a turbulent free-shear layer; this free-shear layer can transfer momentum to the flow near the wall and cause the re-attachment of the flow [17]. Here, the presence/absence of a separation bubble may be responsible for the sharp rise in lift coefficient from $\alpha=25°$ to 30° that we observed in most of our physical models. Indeed, the backbone model was the only model that did not display a discontinuity; the 'backbone' may have disrupted the formation of the separation bubble in the boundary layer, resulting in comparatively lower lift coefficients. However, our flow visualization technique was insufficient to identify fine-scale features in the boundary layer. Future studies using particle image velocimetry (PIV) are planned to test this hypothesis.

Tandem Models

A few studies have examined tandem airfoils at moderate Reynolds numbers, ranging from $Re=8.5\times10^4$ to $Re=2.25\times10^5$ [18–20]. The present study is the first, to our knowledge, to explore the effects of tandem airfoils at Re=15,000. Results from these prior studies are not directly comparable to the present study due to differences in the experimental configurations, including airfoil shape, horizontal and vertical spacing, angle of attack, and Reynolds number. Despite these differences, a few commonalities are noteworthy. Scharpf and Mueller [18] report decreases in lift and drag coefficients of the downstream airfoil when it was spaced horizontally 1.5 chord widths directly behind the upstream model. We observed similarly reduced lift and drag coefficients in our tandem model data in multiple configurations. In both studies, force coefficient reduction was strongest when the downstream model was directly behind the upstream model, which may be explained by the lower airspeed the downstream model experiences in the wake, or by the lower effective angle of attack of the downstream model due to the downwash of the upstream model.

The most interesting effect seen in our tandem model data was the increase of lift coefficient and L/D ratio that occurred in some configurations in which the downstream model was displaced vertically below the upstream model. The flow visualization data suggest two explanations. First, the upstream model's wake appeared to increase the speed of the air directly over the downstream model. Assuming laminar flow in the region outside the turbulent wake and boundary layer, an increase in flow speed implies a local drop in pressure above the downstream model, which would increase the lift force. Second, the wake appeared to deflect the freestream air upward at the leading edge of the downstream model, effectively increasing the angle of attack the model experienced. Because the downstream model was oriented at an angle of attack (25°) less than the angle of maximum lift coefficient (30°), an effective increase in angle of attack would increase the lift coefficient, up to a maximum of 13%. Additionally, the upstream segment's wake may have changed the separation point on the downstream model; unfortunately, our visualization data are not sufficient to establish this point. The maximum increases in lift coefficient (26%) and L/D ratio (54%) occurred at a vertical and horizontal displacement of −0.9 and 3 chord widths, respectively, and these displacement values do indeed occur in real gliding snakes [11].

The interaction effects exhibited by the tandem models in this study may help explain particular unique features of flying snake kinematics. When gliding, the snake's fore body is oriented roughly parallel to the horizontal. In contrast, the rear body moves cyclically in and out of the horizontal plane formed by fore body, an oscillation that occurs at approximately 1 Hz [11]. At times during this vertical cycling, a rear body segment will lie directly behind a fore body segment in the horizontal plane. Because gliding snakes descend at a non-zero glide angle, the air flows past the body at an angle to the horizontal equivalent to the glide angle. In the reference frame of the relative air flow, the downstream (posterior) segment of the snake's body will lie behind and slightly below the upstream (anterior) segment; this staggered configuration is similar to those that produce increased lift coefficients in the downstream tandem model [Fig. 6(b, f)].

Our data open the possibility that the vertical cycling of the rear body could be explained by differences in the lift forces experienced by upstream and downstream body segments. The tandem model results indicate that the relative lift on the downstream body segment will change as the vertical displacement between the upstream and downstream segments of the snake's body change (Fig. 6).

The downstream model (or posterior body segment) encounters lower relative air speeds and reduced lift when it is in the wake of the upstream model [Fig. 6(b)]; this reduced lift might then cause the downstream segment to drop relative to the upstream segment. As the downstream segment falls below the upstream segment, it would experience greater air speed and thus increased relative lift, which would cause it to move up relative to the upstream model. Such an interaction might lead the downstream or posterior segment into a cyclic motion. Note, however, that such a mechanism would explain the oscillation of the posterior (downstream) but not the anterior (upstream) segment only if the center of mass of the snake fell in the upstream segment (so the oscillations occurred around an axis that lay in the upstream segment), or if the two segments were functionally uncoupled. Available data cannot test either corollary, so the possibility that the vertical oscillation of the posterior body segment is actively controlled by the animal cannot be excluded.

Lastly, it is relevant to note that, due to equipment limitations, our study recorded forces only on the downstream model. We did not examine the effects of the downstream model on the upstream model, and these effects can be significant. For example, Scharpf and Mueller [18] reported increases in lift coefficient and decreases in drag coefficient on the upstream airfoil in certain configurations at Reynolds numbers of 8.5×10^4 and 2×10^5. They attributed decreases in drag coefficient on the upstream airfoil to an increase in static pressure between the airfoils, which would reduce drag by lowering the pressure difference between the leading and trailing edges of the upstream airfoil.

Comparison with Real Snakes

This research represents the first study of flying snake aerodynamics. To isolate the aerodynamic effects of certain aspects of cross-sectional shape, a number of simplifications were made, and it is reasonable to ask how well our results compare to limited data from real snakes.

A previous study of flying snake kinematics [11] used measured glide speed and projected body area to estimate whole-body lift and drag coefficients (using equation 2). This calculation assumed that the snakes were gliding at equilibrium (i.e., steady-state) to determine the total lift force on the animal. Snake gliding performance is size-dependant; for example, smaller snakes are capable of gliding farther and at slower speeds than do larger snakes, as would be expected from simple scaling considerations [10]. Socha et al. [11] therefore calculated force coefficients for a representative small and large snake, yielding values of C_L=0.63 and 0.53 and C_D=0.23 and 0.44, respectively, which correspond to lift-to-drag ratios of 2.7 and 1.2. These values are not fully consistent with the model data in this study. Socha et al.'s [11] calculated lift and drag coefficients do not precisely correspond to any single data point for any of our tested models; for example, the large snake's C_L (0.53) occurs at roughly α=10° for the half-full model [Fig. 3(a)], whereas the same snake's C_D (0.44) occurs at roughly α=20° in the same model. Complicating this comparison is the assumption of equilibrium gliding in the real snakes. Equilibrium gliding, in which the total upward aerodynamic force equals the body weight of the animal, has been reported in a gliding mammal (colugo, [21]) and multiple gliding lizards (*Draco* species, [1]), but has not been conclusively shown for a gliding snake. If the snakes reported in Socha et al. [11] did not achieve equilibrium, as seems likely, then the estimated lift and drag coefficients are not appropriate for comparison to our data.

The two L/D ratio values from Socha et al. [11] are within the range of L/D ratios of this study, but that similarity may be coincidental. Plotted on the half-full model data [Fig. 3(d)], the large snake's L/D ratio (1.2) would occur at α=5°; this angle of attack has not been observed in real gliding snakes. The small snake's L/D ratio (2.7) compares favorably to the half-full model data within the range of α=10° to 30° [Fig. 3(d)], but the small snake's lower glide speed (7 vs. 10 $m s^{-1}$) and smaller chord width (1.2 vs. 2.4 cm) put it in a Reynolds number regime (Re= 5,000) lower than that investigated in this study (Re= 15,000). As discussed previously, the sensitivity of airfoil characteristics to Reynolds number suggests that the similarity between the estimate of L/D ratio for the small snake and our data should be viewed with caution. Lastly, Socha et al. [11] reported a maximum estimated L/D ratio of 4.2, which is almost 50% larger any model in the present study. Again, this estimate is derived from a smaller snake operating at a lower Reynolds number than that used in this study, warranting caution in interpretation.

Overall, we conclude that the current data are insufficient to judge the contribution of 2D static airfoil measurements to the explanation of real flying snake aerodynamics. Both work with live animals and modeling efforts require further work, including live animal testing to determine fine-scale kinematic details, more sophisticated fluid mechanical modeling, more realistic physical models, and measurement of airflow patterns around real snakes while gliding. To acquire a comprehensive understanding of the snake's whole-body gliding performance, future studies must address the following issues:

1) *Variation of cross-sectional airfoil shape and size along the body.* In this study we examined one airfoil shape at one Reynolds number. In a real gliding snake, neither the cross-sectional shape nor the body width is constant. The snake's chord is greatest near mid-body,

and body width tapers toward the tail. This changing width has the effect of decreasing the unit projected area and lowering the local Reynolds number along the snake. As the body width decreases (likely due to decreasing rib length), the ventral surface becomes less 'lipped' to the point of being entirely 'full'. Our data show that this should decrease the lift coefficient along the body. Additionally, it is possible that the snake dynamically changes its cross-sectional shape during flight via rib movement, although video records indicate that such changes, if any, are likely to be subtle. In combination, these features emphasize that cross-sectional shape and size must be considered locally throughout the snake's length and glide behavior.

2) *Body movement*. As the snake glides, it constantly changes body posture by sending lateral traveling waves down the body toward the tail. Although undulation frequency does not correlate with any glide performance metric [10] and the ratio of forward speed to undulation speed is high (advance ratio = 42) [11], the snake's cyclic body reconfiguration must produce changes in airflow patterns *per se*. As shown here, the movement of body segments in and out of the wake created by forebody segments will have large effects on the snake's aerodynamics. Furthermore, this body movement will produce a constantly changing location of the center of mass, affecting the snake's aerodynamic stability. The tail, which accounts for roughly 25% of total snake length and moves in an unknown pattern, must be considered as well. The tail has no ribs and therefore remains rounded in cross-sectional shape while gliding. Essentially, the gliding snake is a flattened cylinder with a rounded cylinder projecting from the end; this moving cylinder may create vortices that significantly alter the balance of forces on the snake.
3) *Curvature of the body*. The snake's lateral traveling waves result in an S-like body shape when viewed from above [Fig. 6(d)], with straight sections connected by four to five curves at any one time. This study modeled only the straight sections, but the curved sections likely have significant effects on the snake's aerodynamics. Along a curve, the orientation of the snake's downward-facing 'lips' changes continuously from orthogonal to the flow at the base of a curve, to parallel to the flow at the apex of the curve, and then back to orthogonal at the next straight section. At the apex of the curve, the lateral 'lips' are located to the *sides* of the body, in contrast to the leading and trailing edge configuration studied here; in the curved sections, the body can be roughly considered as a half-cylinder oriented parallel to the flow, and the effect of the lips in the curve are likely to be profoundly different than in the straight sections of the snake. In particular, the body curves will play a critical role in producing (or suppressing) tip vortices, whereas the straight segments will not.
4) *Differential angle of attack among body segments*. The angles of attack modeled in this study encompass the range experienced by real snakes in a typical glide trajectory. After the ballistic dive phase, in which the body undergoes a dramatic change in orientation, the snake's fore body experiences a decreasing angle of attack as the glide trajectory shallows (from roughly $\alpha = 50°$ to 20°), whereas that of the rear body oscillates (roughly through $\alpha = 20°$ to 90°). However, these orientation values were calculated in a previous study [11] using three points on the snake's body, and these body orientation angles do not necessarily correspond to local angles of attack at each body segment. True local angles of attack are not known, and in fact may vary continuously along the body. Although snakes have little capacity for twisting along the backbone axis due to plate-like bony processes (zygapophyses) that essentially restrict vertebral joints to 2D rotation [22], broader body twist can be achieved through sequential bending at each joint, providing the morphological potential to vary angle of attack along the body.

Acknowledgements We thank Mark Stremler, Saad Ragab, and Mark Cramer for helpful discussions on the aerodynamic data in this study, and Pavlos Vlachos for a critical reading of the manuscript and advice. The comments of two anonymous reviewers greatly improved the manuscript. This project was part of an undergraduate honors research thesis (KM) at the University of Chicago; thanks to Heinrich Jaeger and Henry Frisch for their support and advice.

References

1. McGuire JA, Dudley R (2005) The cost of living large: comparative gliding performance in flying lizards (Agamidae: *Draco*). Am Nat 166(1):93–106
2. Jackson SM (1999) Glide angle in the genus *Petaurus* and a review of gliding in mammals. Mamm Rev 30(1):9–30
3. Ando M, Shiraishi S (1993) Gliding flight in the Japanese giant flying squirrel *Petaurista leucogenys*. J Mammal Soc Jpn 18 (1):19–32
4. Scheibe JS, Robins JH (1998) Morphological and performance attributes of gliding mammals. In: Merritt JF, Zegers DA (eds) Ecology and evolutionary biology of tree squirrels. Virginia Museum of Natural History, Martinsville, pp 131–144
5. Vernes K (2001) Gliding performance of the northern flying squirrel (*Glaucomys sabrinus*) in mature mixed forest of Eastern Canada. J Mammal 82(4):1026–1033
6. Stafford BJ, Thorington RW, Kawamichi T (2002) Gliding behavior of Japanese giant flying squirrels (*Petaurista leucogenys*). J Mammal 83(2):553–562
7. Bishop KL (2006) The relationship between 3-D kinematics and gliding performance in the southern flying squirrel, *Glaucomys volans*. J Exp Biol 209(4):689–701
8. Yanoviak SP, Dudley R, Kaspari M (2005) Directed aerial descent in canopy ants. Nature 433(7026):624–626

9. Socha JJ (2002) Gliding flight in the paradise tree snake. Nature 418:603–604
10. Socha JJ, LaBarbera M (2005) Effects of size and behavior on aerial performance of two species of flying snakes (*Chrysopelea*). J Exp Biol 208(10):1835–1847
11. Socha JJ, O'Dempsey T, LaBarbera M (2005) A 3-D kinematic analysis of gliding in a flying snake, *Chrysopelea paradisi*. J Exp Biol 208(10):1817–1833
12. Hoerner SF (1965) Fluid-dynamic drag. Hoerner Fluid Dynamics, Brick Town
13. Spalart PR, Allmaras SR (1992) A one-equation turbulence model for aerodynamic flows. AIAA Conference Paper 1992–439, Reno, NV, pp. 1–22. (Aerospace Sciences Meeting and Exhibit, 30th, Reno, NV, Jan 6–9)
14. Hoerner SF, Borst HV (1975) Fluid-dynamic lift. Hoerner Fluid Dynamics, Brick Town
15. Spedding GR, Hedenstrom AH, McArthur J, Rosen M (2008) The implications of low-speed fixed-wing aerofoil measurements on the analysis and performance of flapping bird wings. J Exp Biol 211(2):215–223
16. Mueller TJ, DeLaurier JD (2003) Aerodynamics of small vehicles. Annu Rev Fluid Mech 35:89–111
17. Torres GE, Mueller TJ (2001) Aerodynamic characteristics of low aspect ratio wings at low Reynolds numbers, in fixed and flapping wing aerodynamics for micro air vehicle applications. Reston, AIAA, pp 115–141
18. Scharpf DF, Mueller TJ (1992) Experimental study of a low Reynolds number tandem airfoil configuration. J Aircraft 29 (2):231–236
19. Michelsen WD, Mueller TJ (1987) Low Reynolds number airfoil performance subjected to wake interference from an upstream airfoil. AIAA Conference Paper 87–2351, Monterey, CA, pp 196–206. (AIAA Applied Aerodynamics Conference, Monterey, California, August 17–19, 1987)
20. Husain Z, Abdullah MZ (2005) Two-dimensional analysis of tandem/staggered airfoils using computational fluid dynamics. Int J Mech Eng Educ 33(3):195–207
21. Byrnes G, Lim NTL, Spence AJ (2008) Take-off and landing kinetics of a free-ranging gliding mammal, the Malayan colugo (*Galeopterus variegatus*). Proc R Soc, B Biol Sci 275(1638):1007–1013
22. Moon BR (1999) Testing an inference of function from structure: snake vertebrae do the twist. J Morphol 241(3): 217–225